

Harmonic Stability Assessment of Multiterminal DC (MTDC) Systems Based on the Hybrid AC/DC Admittance Model and Determinant-Based GNC

Haitao Zhang[✉], *Student Member, IEEE*, Xiuli Wang, *Senior Member, IEEE*,
 Mahmoud Mehrabankhomartash[✉], *Student Member, IEEE*, Maryam Saeedifard[✉], *Senior Member, IEEE*,
 Yongqing Meng, and Xifan Wang, *Life Fellow, IEEE*

Abstract—Growing concerns with the harmonic oscillation phenomenon of multiterminal DC (MTDC) systems calls for appropriate harmonic stability analysis methods. However, the conventional ac or dc admittance-based stability assessment methods cannot effectively protect trade secret and user privacy, distinguish different system instability root causes, and put forward corresponding instability mitigation methods. To address the aforementioned issues, this article first establishes a hybrid ac/dc admittance-based stability assessment model for a MTDC system. Then, by introducing the determinant-based General Nyquist Criterion (GNC), the system stability is assessed and three types of instability root causes, including the ac side, the dc side, and the coupling interaction between the ac and dc sides are identified. Regarding the instability caused by the ac side, the dominant interlinking converter is directly identified, in which the instability can be mitigated by reshaping its q-axis admittance. In contrast, for the instability caused by the latter two root causes, the most influential interlinking converter is recognized by an additional sensitivity analysis. The instability is then mitigated by reshaping the dc-side equivalent admittance of the most influential interlinking converter. Compared with the conventional methods, the proposed method offers advantages as follows: 1) trade secret and user privacy is effectively protected, 2) different system instability root causes can be effectively distinguished, and 3) instabilities caused by diverse root causes can be mitigated by corresponding methods. Finally, the proposed method is verified by simulations in the MATLAB/Simulink environment.

Index Terms—Determinant-based GNC, harmonic stability, hybrid ac/dc admittance, impedance-based stability assessment, MTDC system.

Manuscript received February 13, 2021; revised May 6, 2021 and June 27, 2021; accepted August 2, 2021. Date of publication August 10, 2021; date of current version October 15, 2021. This work was supported by the Technology Foundation of SGEPRI's Research on Experimental Study on the Multi-terminal Hybrid DC Transmission System (SGNR0000KJJS2000649). Recommended for publication by Associate Editor X. Wang. (*Corresponding author: Haitao Zhang.*)

Haitao Zhang, Xiuli Wang, Yongqing Meng, and Xifan Wang are with the School of Electrical Engineering, Xi'an Jiaotong University, Xi'an, Shaanxi 710049, China (e-mail: htzhangee@gmail.com; xiuliw@mail.xjtu.edu.cn; mengyq@mail.xjtu.edu.cn; xfwang@mail.xjtu.edu.cn).

Mahmoud Mehrabankhomartash and Maryam Saeedifard are with the School of Electrical and Computer Engineering, Georgia Institute of Technology, Atlanta, GA 30332-0002 USA (e-mail: mehraban.mahmoud@gatech.edu; maryam@ece.gatech.edu).

Color versions of one or more figures in this article are available at <https://doi.org/10.1109/TPEL.2021.3103797>.

Digital Object Identifier 10.1109/TPEL.2021.3103797

I. INTRODUCTION

MULTITERMINAL dc (MTDC) systems have become a key technology in realization of meshed ac/dc grids [1]–[3] as they offer enormous advantages for interconnection of asynchronous grids, wind power integration, offshore platform power supply, and urban power supply. However, with large-scale integration of interlinking converters, the issues associated with harmonic instability have gradually become prominent and noted in several projects worldwide [4], [5]. To assess the stability of MTDC systems, the two commonly used methods are the time-domain state-space analysis method [6], [7] and the frequency-domain impedance analysis method [8]–[10]. Compared with the former one, the impedance analysis method regards the analysis target as a “black-box” and assesses system stability with only the external measured admittance or impedance [11], [12]. Therefore, especially in the current power market environment, it can effectively protect trade secret and user privacy, and has been utilized in many related technical literature.

Corresponding to two different admittance models, i.e., the ac and dc impedances, the stability assessment of a MTDC system is usually conducted either on the ac side [13], [14] or the dc side [15]–[17]. Although significant work has been done, the ac and dc admittance-based stability assessment methods both encounter several problems as follows. First, the components in a MTDC system cannot be viewed as “black-boxes” anymore. For example, the dc admittance of an interlinking converter is usually impacted by the impedance of the connected ac grid [18], [19]. When an interlinking converter is embedded within different ac grids, the general assumption that the converter is stable when it operates standalone cannot guarantee that its dc admittance does not contain any right half-plane (RHP) pole. Therefore, detailed internal control structure and parameters are needed to calculate the number of RHP poles of the dc admittance. Although some estimation methods have been proposed [20], visual examination of the encirclement of $(-1, j0)$ point is still challenging [21]. Second, the interactions between the ac and dc sides of a MTDC system are difficult to investigate and various instability root causes are not trivial to distinguish. As noted in [22], the stability assessment results obtained from the ac and dc sides are identical. Therefore, when either of the ac or dc

where $\tilde{u}_{di}(\tilde{u}_{qi})$, $\tilde{v}_{di}(\tilde{v}_{qi})$, and $\tilde{i}_{di}(\tilde{i}_{qi})$ represent the small-signal values of $u_{di}(u_{qi})$, $v_{di}(v_{qi})$, and $i_{di}(i_{qi})$, respectively. $\mathbf{Z}_{\text{grid}i}^{\text{ac}}$ represents the impedance matrix of the i th ac grid and is expressed by

$$\mathbf{Z}_{\text{grid}i}^{\text{ac}} = \begin{bmatrix} sL_i + R_i & -\omega L_i \\ \omega L_i & sL_i + R_i \end{bmatrix} \quad (2)$$

where ω represents the angular-frequency of the i th ac grid. In addition, the dc network is described by

$$\begin{bmatrix} \tilde{v}_{dc1} \\ \tilde{v}_{dc2} \\ \vdots \\ \tilde{v}_{dcn} \end{bmatrix} = \begin{bmatrix} Z_{\text{net}11}^{\text{dc}} & Z_{\text{net}12}^{\text{dc}} & \cdots & Z_{\text{net}1n}^{\text{dc}} \\ Z_{\text{net}21}^{\text{dc}} & Z_{\text{net}22}^{\text{dc}} & \cdots & Z_{\text{net}2n}^{\text{dc}} \\ \vdots & \vdots & \ddots & \vdots \\ Z_{\text{net}n1}^{\text{dc}} & Z_{\text{net}n2}^{\text{dc}} & \cdots & Z_{\text{net}nn}^{\text{dc}} \end{bmatrix} \begin{bmatrix} -\tilde{i}_{dc1} \\ -\tilde{i}_{dc2} \\ \vdots \\ -\tilde{i}_{dcn} \end{bmatrix} \quad (3)$$

where \tilde{v}_{dci} , \tilde{i}_{dci} , $Z_{\text{net}ii}^{\text{dc}}$ ($i = 1, 2, \dots, n$), and $Z_{\text{net}ij}^{\text{dc}}$ ($i, j = 1, 2, \dots, n, i \neq j$) represent the small-signal value of v_{dci} , the small-signal value of i_{dci} , the self-impedance of the node i , and the mutual-impedance between the nodes i and j , respectively.

On the basis of (1), (2), and (3), the ac grids and the dc network are collectively modeled and the small-signal model of the first subsystem is described by

$$\tilde{\mathbf{u}}_{\text{acdc}} = \mathbf{Z}_{\text{sub}1} \tilde{\mathbf{i}}_{\text{acdc}} + \tilde{\mathbf{v}}_{\text{acdc}} \quad (4)$$

where $\tilde{\mathbf{u}}_{\text{acdc}}$, $\tilde{\mathbf{i}}_{\text{acdc}}$, $\tilde{\mathbf{v}}_{\text{acdc}}$, and $\mathbf{Z}_{\text{sub}1}$ are defined in (5), (6), (7), and (8), respectively. To distinguish the variables belonging to the ac side from that of the dc side, the variables in $\tilde{\mathbf{u}}_{\text{acdc}}$, $\tilde{\mathbf{i}}_{\text{acdc}}$, and $\tilde{\mathbf{v}}_{\text{acdc}}$ are divided with dashed lines. Correspondingly, $\mathbf{Z}_{\text{sub}1}$ is also divided into four matrix blocks. The upper left matrix block and the lower right one are labeled as $\mathbf{Z}_{\text{sub}1}^{\text{ac}}$ and $\mathbf{Z}_{\text{sub}1}^{\text{dc}}$, which represent the ac impedance matrix and dc impedance matrix of the first subsystem, respectively. The admittance matrix of the first subsystem $\mathbf{Y}_{\text{sub}1}$, i.e., the inverse matrix of $\mathbf{Z}_{\text{sub}1}$ is defined in (9)

$$\tilde{\mathbf{u}}_{\text{acdc}} = [\tilde{u}_{d1} \ \tilde{u}_{q1} \ \tilde{u}_{d2} \ \tilde{u}_{q2} \ \cdots \ \tilde{u}_{dn} \ \tilde{u}_{qn} \ 0 \ 0 \ \cdots \ 0]^T \quad (5)$$

$$\tilde{\mathbf{i}}_{\text{acdc}} = [\tilde{i}_{d1} \ \tilde{i}_{q1} \ \tilde{i}_{d2} \ \tilde{i}_{q2} \ \cdots \ \tilde{i}_{dn} \ \tilde{i}_{qn} \ \tilde{i}_{dc1} \ \tilde{i}_{dc2} \ \cdots \ \tilde{i}_{dcn}]^T \quad (6)$$

$$\tilde{\mathbf{v}}_{\text{acdc}} = [\tilde{v}_{d1} \ \tilde{v}_{q1} \ \tilde{v}_{d2} \ \tilde{v}_{q2} \ \cdots \ \tilde{v}_{dn} \ \tilde{v}_{qn} \ \tilde{v}_{dc1} \ \tilde{v}_{dc2} \ \cdots \ \tilde{v}_{dcn}]^T, \quad (7)$$

$$\mathbf{Z}_{\text{sub}1} = \begin{bmatrix} \mathbf{Z}_{\text{sub}1}^{\text{ac}} & \mathbf{0} \\ \mathbf{0} & \mathbf{Z}_{\text{sub}1}^{\text{dc}} \end{bmatrix} = \begin{bmatrix} \mathbf{Z}_{\text{grid}1}^{\text{ac}} & \mathbf{0} & \cdots & \mathbf{0} & \mathbf{0} & \mathbf{0} & \cdots & \mathbf{0} \\ \mathbf{0} & \mathbf{Z}_{\text{grid}2}^{\text{ac}} & \cdots & \mathbf{0} & \mathbf{0} & \mathbf{0} & \cdots & \mathbf{0} \\ \vdots & \vdots & \ddots & \vdots & \vdots & \vdots & \ddots & \vdots \\ \mathbf{0} & \mathbf{0} & \cdots & \mathbf{Z}_{\text{grid}n}^{\text{ac}} & \mathbf{0} & \mathbf{0} & \cdots & \mathbf{0} \\ \mathbf{0} & \mathbf{0} & \cdots & \mathbf{0} & Z_{\text{net}11}^{\text{dc}} & Z_{\text{net}12}^{\text{dc}} & \cdots & Z_{\text{net}1n}^{\text{dc}} \\ \mathbf{0} & \mathbf{0} & \cdots & \mathbf{0} & Z_{\text{net}21}^{\text{dc}} & Z_{\text{net}22}^{\text{dc}} & \cdots & Z_{\text{net}2n}^{\text{dc}} \\ \vdots & \vdots & \ddots & \vdots & \vdots & \vdots & \ddots & \vdots \\ \mathbf{0} & \mathbf{0} & \cdots & \mathbf{0} & Z_{\text{net}n1}^{\text{dc}} & Z_{\text{net}n2}^{\text{dc}} & \cdots & Z_{\text{net}nn}^{\text{dc}} \end{bmatrix} \quad (8)$$

$$\mathbf{Y}_{\text{sub}1} = \begin{bmatrix} \mathbf{Y}_{\text{sub}1}^{\text{ac}} & \mathbf{0} \\ \mathbf{0} & \mathbf{Y}_{\text{sub}1}^{\text{dc}} \end{bmatrix} = \begin{bmatrix} \mathbf{Y}_{\text{grid}1}^{\text{ac}} & \mathbf{0} & \cdots & \mathbf{0} & \mathbf{0} & \mathbf{0} & \cdots & \mathbf{0} \\ \mathbf{0} & \mathbf{Y}_{\text{grid}2}^{\text{ac}} & \cdots & \mathbf{0} & \mathbf{0} & \mathbf{0} & \cdots & \mathbf{0} \\ \vdots & \vdots & \ddots & \vdots & \vdots & \vdots & \ddots & \vdots \\ \mathbf{0} & \mathbf{0} & \cdots & \mathbf{Y}_{\text{grid}n}^{\text{ac}} & \mathbf{0} & \mathbf{0} & \cdots & \mathbf{0} \\ \mathbf{0} & \mathbf{0} & \cdots & \mathbf{0} & Y_{\text{net}11}^{\text{dc}} & Y_{\text{net}12}^{\text{dc}} & \cdots & Y_{\text{net}1n}^{\text{dc}} \\ \mathbf{0} & \mathbf{0} & \cdots & \mathbf{0} & Y_{\text{net}21}^{\text{dc}} & Y_{\text{net}22}^{\text{dc}} & \cdots & Y_{\text{net}2n}^{\text{dc}} \\ \vdots & \vdots & \ddots & \vdots & \vdots & \vdots & \ddots & \vdots \\ \mathbf{0} & \mathbf{0} & \cdots & \mathbf{0} & Y_{\text{net}n1}^{\text{dc}} & Y_{\text{net}n2}^{\text{dc}} & \cdots & Y_{\text{net}nn}^{\text{dc}} \end{bmatrix}. \quad (9)$$

B. Small-Signal Model of the Second Subsystem

Based on the hybrid ac/dc admittance model developed in [23], the i th interlinking converter is described by

$$\begin{bmatrix} \tilde{i}_{di} \\ \tilde{i}_{qi} \\ \tilde{i}_{dci} \end{bmatrix} = \begin{bmatrix} \mathbf{Y}_{\text{con}i}^{\text{ac}} & \mathbf{Y}_{\text{con}i}^{\text{acdc}} \\ \mathbf{Y}_{\text{con}i}^{\text{dcac}} & Y_{\text{con}i}^{\text{dc}} \end{bmatrix} \begin{bmatrix} \tilde{v}_{di} \\ \tilde{v}_{qi} \\ \tilde{v}_{dci} \end{bmatrix} \quad (10)$$

where $\mathbf{Y}_{\text{con}i}^{\text{ac}}$, $\mathbf{Y}_{\text{con}i}^{\text{acdc}}$, $\mathbf{Y}_{\text{con}i}^{\text{dcac}}$, and $Y_{\text{con}i}^{\text{dc}}$ represent the ac admittance matrix, the coupling admittance matrices between the ac and dc sides, and the dc admittance of the i th interlinking converter, respectively. The former three admittance matrices are defined as follows:

$$\mathbf{Y}_{\text{con}i}^{\text{ac}} = \begin{bmatrix} Y_{ddi}^c & Y_{dqi}^c \\ Y_{qdi}^c & Y_{qqi}^c \end{bmatrix} \quad (11)$$

$$\mathbf{Y}_{\text{con}i}^{\text{acdc}} = [Y_{ddci}^c \ Y_{qdci}^c]^T \quad (12)$$

$$\mathbf{Y}_{\text{con}i}^{\text{dcac}} = [Y_{dcdi}^c \ Y_{dcqi}^c]. \quad (13)$$

By collective modeling, all the interlinking converters together with the hybrid ac/dc admittance model and separating the ac- and dc-side variables, the second subsystem is modeled by

$$\tilde{\mathbf{i}}_{\text{acdc}} = \mathbf{Y}_{\text{sub}2} \tilde{\mathbf{v}}_{\text{acdc}} \quad (14)$$

where $\mathbf{Y}_{\text{sub}2}$ represents the hybrid ac/dc admittance matrix of the second subsystem and is defined by (15) shown at the bottom of next page. With respect to (15), $\mathbf{Y}_{\text{sub}2}$ is divided into four matrix blocks with dotted lines. The upper left part, the upper right part, the lower left part, and the lower right parts are denoted by $\mathbf{Y}_{\text{sub}2}^{\text{ac}}$, $\mathbf{Y}_{\text{sub}2}^{\text{acdc}}$, $\mathbf{Y}_{\text{sub}2}^{\text{dcac}}$, and $\mathbf{Y}_{\text{sub}2}^{\text{dc}}$, which represent the ac admittance matrix, the coupling admittance matrices between the ac and dc sides, and the dc admittance matrix of the second subsystem, respectively.

C. Stability Assessment of the MTDC System

By substituting for $\tilde{\mathbf{i}}_{\text{acdc}}$ from (14) into (4), the small-signal model of the MTDC system is expressed by

$$\tilde{\mathbf{v}}_{\text{acdc}} = (\mathbf{I} + \mathbf{Z}_{\text{sub}1} \mathbf{Y}_{\text{sub}2})^{-1} \tilde{\mathbf{u}}_{\text{acdc}} \quad (16)$$

where \mathbf{I} represents an identity matrix. Based on (16), the system minor-loop gain \mathbf{L} is defined as

$$\mathbf{L} = \mathbf{Z}_{\text{sub}1} \mathbf{Y}_{\text{sub}2}. \quad (17)$$

Since the impedances of the ac grids and the dc network consist of only passive elements such as resistance, inductance, and capacitance, the impedance matrix of the first subsystem, i.e., \mathbf{Z}_{sub1} does not contain any RHP pole. Moreover, with the general assumption that all the interlinking converters are stable when they operate standalone, the admittance matrix of the second subsystem, i.e., \mathbf{Y}_{sub2} does not contain any RHP pole as well. Therefore, the system minor-loop gain defined by (17) does not contain any RHP pole. By defining the determinant of the return-difference matrix, i.e., $|\mathbf{F}|$ as

$$|\mathbf{F}| = |\mathbf{I} + \mathbf{L}| = |\mathbf{I} + \mathbf{Z}_{\text{sub1}} \mathbf{Y}_{\text{sub2}}| \quad (18)$$

based on the determinant-based GNC [25]–[27], the stability of the MTDC system can be determined by checking whether the phase angle of $|\mathbf{F}|$ decreases by more than 180° when the frequency increases from 0 to infinity. To be more specific, if the phase angle decrement of $|\mathbf{F}|$ is 0° over the entire positive frequency range, the closed-loop system does not contain any RHP pole, and therefore the MTDC system is stable. In contrast, if the phase angle of $|\mathbf{F}|$ decreases by $n \times 180^\circ$, the closed-loop system contains n RHP poles, and consequently the MTDC system is unstable.

III. INSTABILITY ROOT CAUSE IDENTIFICATION AND MITIGATION

With the model formulated in Section II, the stability of a MTDC system can be assessed by checking whether the phase angle of $|\mathbf{F}|$ decreases more than 180° when the frequency increases from 0 to infinity. Therefore, to investigate the instability root cause of an unstable MTDC system, the component that causes the phase angle decrement of $|\mathbf{F}|$ should be identified. To achieve this goal, (8), (9), and (15) are substituted into (18). By the aid of determinant property, the determinant of return-difference matrix $|\mathbf{F}|$ defined in (18) is calculated as (19) shown at the bottom of this page. The $n + 1$ determinants on the right hand of (19) are labeled as $|\mathbf{F}_1|$, $|\mathbf{F}_2|$, \dots , $|\mathbf{F}_n|$, and $|\mathbf{F}_{n+1}|$, respectively. With respect to (19), the determinants on the right hand of (19) are classified into two parts. The first part includes the former n determinants, i.e., $|\mathbf{F}_i|$ ($i = 1, 2, \dots, n$) while the second part refers to the last determinant, i.e., $|\mathbf{F}_{n+1}|$.

Notice that the phase angle of $|\mathbf{F}|$ equals the sum of the phase angles of the first and second parts. Assuming that the system is unstable and the phase angle decrement of $|\mathbf{F}|$ is caused by the first or second part, the root causes of system instability are illustrated from two perspectives in the following sections.

A. Instability Root Cause Identification and Mitigation of the AC Side

Prior to analyzing the instability root cause of the ac side, the physical implications of the determinants of the first part, i.e., $|\mathbf{F}_i|$ ($i = 1, 2, \dots, n$) are initially illustrated. Taking $|\mathbf{F}_1|$ as an example, it is rewritten as

$$|\mathbf{F}_1| = |\mathbf{I} + \mathbf{Z}_{\text{grid1}}^{\text{ac}} \mathbf{Y}_{\text{con1}}^{\text{ac}}|, (i = 1, 2, \dots, n). \quad (20)$$

Note that $\mathbf{Z}_{\text{grid1}}^{\text{ac}}$ and $\mathbf{Y}_{\text{con1}}^{\text{ac}}$ represent the ac impedance matrix of the i th ac grid and the ac admittance matrix of the i th interlinking converter, respectively. Therefore, $\mathbf{Z}_{\text{grid1}}^{\text{ac}} \mathbf{Y}_{\text{con1}}^{\text{ac}}$ is the system minor-loop gain of the i th interlinking converter on the ac side. $|\mathbf{F}_1|$ is the corresponding determinant of return-difference matrix, which determines the ac-side stability of the i th interlinking converter.

According to the above analysis, every determinant of the first part corresponds to the ac-side stability of an interlinking converter. Hence, the first part represents the ac-side stability of a MTDC system. For an unstable MTDC system, if the phase angle decrement of $|\mathbf{F}|$ is caused by one or several determinants of the first part, it is concluded that the system instability is caused by the ac side of the MTDC system. Furthermore, the specific interlinking converter that triggers the instability can be further identified by checking which determinant within the first part, i.e., $|\mathbf{F}_i|$, ($n = 1, 2, \dots, n$), causes the phase angle decrement of $|\mathbf{F}|$. For example, suppose that as the frequency increases from 0 to infinity, only $|\mathbf{F}_2|$ and $|\mathbf{F}|$ have a phase angle reduction of more than 180° , while the other determinants have no phase angle reduction. On the grounds of the aforementioned analysis, this MTDC system is unstable and the instability is caused by the ac side of the second interlinking converter.

To mitigate the instability caused by the ac side, the q -axis admittance of the instability-causing interlinking converter should be reshaped to be positive or less negative [11], [28].

$$\mathbf{Y}_{\text{sub2}} = \begin{bmatrix} \mathbf{Y}_{\text{sub2}}^{\text{ac}} & \mathbf{Y}_{\text{sub2}}^{\text{dcac}} \\ \mathbf{Y}_{\text{sub2}}^{\text{dcac}} & \mathbf{Y}_{\text{sub2}}^{\text{dc}} \end{bmatrix} = \begin{bmatrix} \mathbf{Y}_{\text{con1}}^{\text{ac}} & \mathbf{0} & \dots & \mathbf{0} & \mathbf{Y}_{\text{con1}}^{\text{dcac}} & \mathbf{0} & \dots & \mathbf{0} \\ \mathbf{0} & \mathbf{Y}_{\text{con2}}^{\text{ac}} & \dots & \mathbf{0} & \mathbf{0} & \mathbf{Y}_{\text{con2}}^{\text{dcac}} & \dots & \mathbf{0} \\ \vdots & \vdots & \ddots & \vdots & \vdots & \vdots & \ddots & \vdots \\ \mathbf{0} & \mathbf{0} & \dots & \mathbf{Y}_{\text{conn}}^{\text{ac}} & \mathbf{0} & \mathbf{0} & \dots & \mathbf{Y}_{\text{conn}}^{\text{dcac}} \\ \mathbf{Y}_{\text{con1}}^{\text{dcac}} & \mathbf{0} & \dots & \mathbf{0} & \mathbf{Y}_{\text{con1}}^{\text{dc}} & \mathbf{0} & \dots & \mathbf{0} \\ \mathbf{0} & \mathbf{Y}_{\text{con2}}^{\text{dcac}} & \dots & \mathbf{0} & \mathbf{0} & \mathbf{Y}_{\text{con2}}^{\text{dc}} & \dots & \mathbf{0} \\ \vdots & \vdots & \ddots & \vdots & \vdots & \vdots & \ddots & \vdots \\ \mathbf{0} & \mathbf{0} & \dots & \mathbf{Y}_{\text{conn}}^{\text{dcac}} & \mathbf{0} & \mathbf{0} & \dots & \mathbf{Y}_{\text{conn}}^{\text{dc}} \end{bmatrix} \quad (15)$$

$$|\mathbf{F}| = \underbrace{|\mathbf{I} + \mathbf{Z}_{\text{grid1}}^{\text{ac}} \mathbf{Y}_{\text{con1}}^{\text{ac}}|}_{|\mathbf{F}_1|} \underbrace{|\mathbf{I} + \mathbf{Z}_{\text{grid2}}^{\text{ac}} \mathbf{Y}_{\text{con2}}^{\text{ac}}|}_{|\mathbf{F}_2|} \dots \underbrace{|\mathbf{I} + \mathbf{Z}_{\text{gridn}}^{\text{ac}} \mathbf{Y}_{\text{conn}}^{\text{ac}}|}_{|\mathbf{F}_n|} \underbrace{|\mathbf{I} + (\mathbf{Y}_{\text{sub2}}^{\text{dc}} - \mathbf{Y}_{\text{sub2}}^{\text{dcac}} (\mathbf{Y}_{\text{sub1}}^{\text{ac}} + \mathbf{Y}_{\text{sub2}}^{\text{ac}})^{-1} \mathbf{Y}_{\text{sub2}}^{\text{dcac}}) \mathbf{Z}_{\text{sub1}}^{\text{dc}}|}_{|\mathbf{F}_{n+1}|} \quad (19)$$

According to the characteristics of hybrid ac/dc admittance, when an interlinking converter operates under high power factor, its q -axis admittance is determined by its q -axis controllers and phase-locked loop (PLL). Therefore, to mitigate the instability caused by the ac side, the parameters of the q -axis controllers or PLL of the instability-causing interlinking converter should be adjusted.

B. Instability Root Cause Identification and Mitigation of the DC Side

Similar to the analysis of the first part, if the second part, i.e., $|\mathbf{F}_{n+1}|$ is considered as a determinant of return-difference matrix, the corresponding system minor-loop gain will be $(\mathbf{Y}_{\text{sub2}}^{\text{dc}} - \mathbf{Y}_{\text{sub2}}^{\text{dcac}}(\mathbf{Y}_{\text{sub1}}^{\text{ac}} + \mathbf{Y}_{\text{sub2}}^{\text{ac}})^{-1}\mathbf{Y}_{\text{sub2}}^{\text{acdc}})\mathbf{Z}_{\text{sub1}}^{\text{dc}}$. Notice that $\mathbf{Y}_{\text{sub2}}^{\text{dc}}$, $\mathbf{Y}_{\text{sub2}}^{\text{dcac}}(\mathbf{Y}_{\text{sub1}}^{\text{ac}} + \mathbf{Y}_{\text{sub2}}^{\text{ac}})^{-1}\mathbf{Y}_{\text{sub2}}^{\text{acdc}}$, and $\mathbf{Z}_{\text{sub1}}^{\text{dc}}$ represent the dc admittance matrix of the second subsystem, the impact term of the ac side of the MTDC system on the dc admittance matrix of the second subsystem, and the dc impedance matrix of the first subsystem, respectively. By regarding $\mathbf{Y}_{\text{sub2}}^{\text{dc}} - \mathbf{Y}_{\text{sub2}}^{\text{dcac}}(\mathbf{Y}_{\text{sub1}}^{\text{ac}} + \mathbf{Y}_{\text{sub2}}^{\text{ac}})^{-1}\mathbf{Y}_{\text{sub2}}^{\text{acdc}}$ as the dc-side equivalent admittance matrix of the second subsystem, the second part, i.e., $|\mathbf{F}_{n+1}|$, describes the dc-side stability and the impact of the coupling interaction between the ac and dc sides on the system stability. Since the instabilities caused by the dc side and the coupling interaction will be mitigated together afterward, the following part does not distinguish between these two instability root causes. They both are renamed as the instability caused by the dc side

Assume that a MTDC system is unstable and the phase angle decrement of $|\mathbf{F}|$ is caused by $|\mathbf{F}_{n+1}|$. Under this condition, the system instability is caused by the dc side of the MTDC system. It is noteworthy that all the interlinking converters are coupled together through the dc network on the dc side. Therefore, the dc-side stability of a MTDC system is determined by the joint effect of all interlinking converters rather than any specific one. The only difference is that their impact varies from one to another. To mitigate the instability caused by the dc side, the dominant interlinking converter that has the most influential impact on the dc-side stability is necessary to recognize first. To this end, the dc-side equivalent admittance of the second subsystem, i.e., $\mathbf{Y}_{\text{sub2}}^{\text{dc}} - \mathbf{Y}_{\text{sub2}}^{\text{dcac}}(\mathbf{Y}_{\text{sub1}}^{\text{ac}} + \mathbf{Y}_{\text{sub2}}^{\text{ac}})^{-1}\mathbf{Y}_{\text{sub2}}^{\text{acdc}}$ is

calculated as (21) shown at the bottom of this page. As shown in (21), $\mathbf{Y}_{\text{sub2}}^{\text{dc}} - \mathbf{Y}_{\text{sub2}}^{\text{dcac}}(\mathbf{Y}_{\text{sub1}}^{\text{ac}} + \mathbf{Y}_{\text{sub2}}^{\text{ac}})^{-1}\mathbf{Y}_{\text{sub2}}^{\text{acdc}}$ is a diagonal matrix. The i th main diagonal element, i.e., $Y_{\text{con}i}^{\text{dc}} - \mathbf{Y}_{\text{con}i}^{\text{dcac}}(\mathbf{Y}_{\text{grid}i}^{\text{ac}} + \mathbf{Y}_{\text{con}i}^{\text{ac}})^{-1}\mathbf{Y}_{\text{con}i}^{\text{acdc}}$ represents the dc-side equivalent admittance of the i th interlinking converter. Hence, the impact of the i th interlinking converter on the dc-side stability can be measured by the sensitivity of $|\mathbf{F}_{n+1}|$ to its dc-side equivalent admittance, i.e., $Y_{\text{con}i}^{\text{dc}} - \mathbf{Y}_{\text{con}i}^{\text{dcac}}(\mathbf{Y}_{\text{grid}i}^{\text{ac}} + \mathbf{Y}_{\text{con}i}^{\text{ac}})^{-1}\mathbf{Y}_{\text{con}i}^{\text{acdc}}$.

To calculate the aforementioned sensitivity, first, the eigenvalues of \mathbf{F}_{n+1} are denoted as $\lambda_1, \lambda_2, \dots$, and λ_n . Then, $|\mathbf{F}_{n+1}|$ is expressed by

$$|\mathbf{F}_{n+1}| = \lambda_1 \lambda_2 \cdots \lambda_n. \quad (22)$$

On the basis of $|\mathbf{F}_{n+1}|$ expressed by (22), the sensitivity of $|\mathbf{F}_{n+1}|$ with respect to the j th eigenvalue, i.e., λ_j is calculated as

$$\frac{\partial |\mathbf{F}_{n+1}|}{\partial \lambda_j} = \lambda_1 \lambda_2 \cdots \lambda_{j-1} \lambda_{j+1} \cdots \lambda_n. \quad (23)$$

In addition, if the left and right eigenvectors of λ_j are defined as \mathbf{r}_j^T and \mathbf{l}_j , the sensitivity of the j th eigenvalue, i.e., λ_j with respect to the dc-side equivalent admittance of the i th interlinking converter, i.e., $Y_{\text{con}i}^{\text{dc}} - \mathbf{Y}_{\text{con}i}^{\text{dcac}}(\mathbf{Y}_{\text{grid}i}^{\text{ac}} + \mathbf{Y}_{\text{con}i}^{\text{ac}})^{-1}\mathbf{Y}_{\text{con}i}^{\text{acdc}}$ is expressed by

$$\begin{aligned} & \frac{\partial \lambda_j}{\partial (Y_{\text{con}i}^{\text{dc}} - \mathbf{Y}_{\text{con}i}^{\text{dcac}}(\mathbf{Y}_{\text{grid}i}^{\text{ac}} + \mathbf{Y}_{\text{con}i}^{\text{ac}})^{-1}\mathbf{Y}_{\text{con}i}^{\text{acdc}})} \\ &= \frac{1}{\mathbf{r}_j^T \mathbf{l}_j} \mathbf{r}_j^T \mathbf{I}_{ii} \mathbf{Z}_{\text{sub1}}^{\text{dc}} \mathbf{l}_j \end{aligned} \quad (24)$$

where \mathbf{I}_{ii} represents a special matrix, whose element in the i th row and column is 1 while all other elements are zero. On the basis of the sensitivities obtained from (23) and (24), the sensitivity of $|\mathbf{F}_{n+1}|$ to the dc-side equivalent admittance of the i th interlinking converter is calculated as (25) shown at the bottom of this page. The most influential interlinking converter can be identified as the one owning the greatest sensitivity.

In contrast to the system instability induced by the ac side, the system instability triggered by the dc side is caused by the dc-side equivalent admittance of interlinking converters. According to the characteristics of hybrid ac/dc admittance, when an interlinking converter operates under high power factor, its dc-side equivalent admittance is determined by the d -axis

$$\begin{aligned} & \mathbf{Y}_{\text{sub2}}^{\text{dc}} - \mathbf{Y}_{\text{sub2}}^{\text{dcac}}(\mathbf{Y}_{\text{sub1}}^{\text{ac}} + \mathbf{Y}_{\text{sub2}}^{\text{ac}})^{-1}\mathbf{Y}_{\text{sub2}}^{\text{acdc}} = \\ & \begin{bmatrix} Y_{\text{con}1}^{\text{dc}} & & & & \\ -\mathbf{Y}_{\text{con}1}^{\text{dcac}}(\mathbf{Y}_{\text{grid}1}^{\text{ac}} + \mathbf{Y}_{\text{con}1}^{\text{ac}})^{-1}\mathbf{Y}_{\text{con}1}^{\text{acdc}} & 0 & \cdots & & 0 \\ 0 & Y_{\text{con}2}^{\text{dc}} - \mathbf{Y}_{\text{con}2}^{\text{dcac}}(\mathbf{Y}_{\text{grid}2}^{\text{ac}} + \mathbf{Y}_{\text{con}2}^{\text{ac}})^{-1}\mathbf{Y}_{\text{con}2}^{\text{acdc}} & \cdots & & 0 \\ \vdots & \vdots & \ddots & & \vdots \\ 0 & 0 & \cdots & Y_{\text{con}n}^{\text{dc}} & -\mathbf{Y}_{\text{con}n}^{\text{dcac}}(\mathbf{Y}_{\text{grid}n}^{\text{ac}} + \mathbf{Y}_{\text{con}n}^{\text{ac}})^{-1}\mathbf{Y}_{\text{con}n}^{\text{acdc}} \end{bmatrix} \end{aligned} \quad (21)$$

$$\frac{\partial |\mathbf{F}_{n+1}|}{\partial (Y_{\text{con}i}^{\text{dc}} - \mathbf{Y}_{\text{con}i}^{\text{dcac}}(\mathbf{Y}_{\text{grid}i}^{\text{ac}} + \mathbf{Y}_{\text{con}i}^{\text{ac}})^{-1}\mathbf{Y}_{\text{con}i}^{\text{acdc}})} = \sum_{j=1}^n \lambda_1 \lambda_2 \cdots \lambda_{j-1} \lambda_{j+1} \cdots \lambda_n \frac{1}{\mathbf{r}_j^T \mathbf{l}_j} \mathbf{r}_j^T \mathbf{I}_{ii} \mathbf{Z}_{\text{sub1}}^{\text{dc}} \mathbf{l}_j, (i = 1, 2, \dots, n) \quad (25)$$

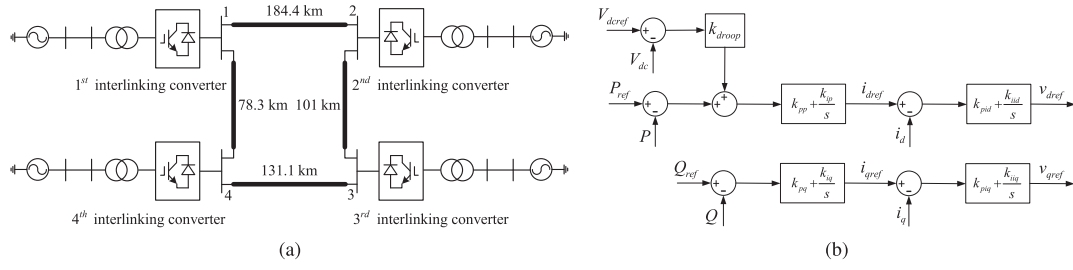


Fig. 2. Circuit diagram and control diagram of the test system. (a) Circuit diagram of the test system. (b) Control diagram of the i th interlinking converter.

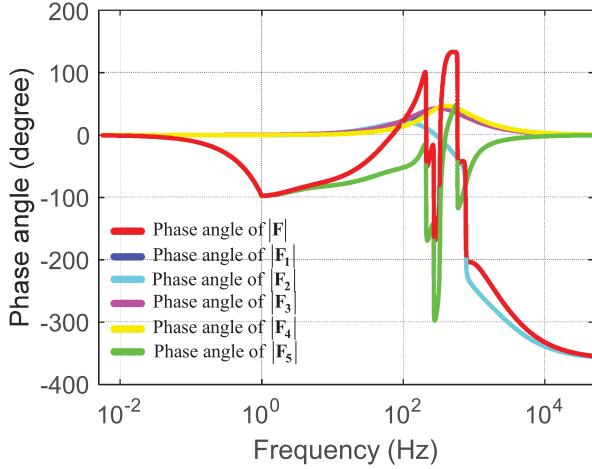


Fig. 3. Phase angles of $|F|$, $|F_1|$, $|F_2|$, $|F_3|$, $|F_4|$, and $|F_5|$ with $k_{pq2} = 1.42 \times 10^{-5}$ and $k_{iq2} = 1.42 \times 10^{-4}$.

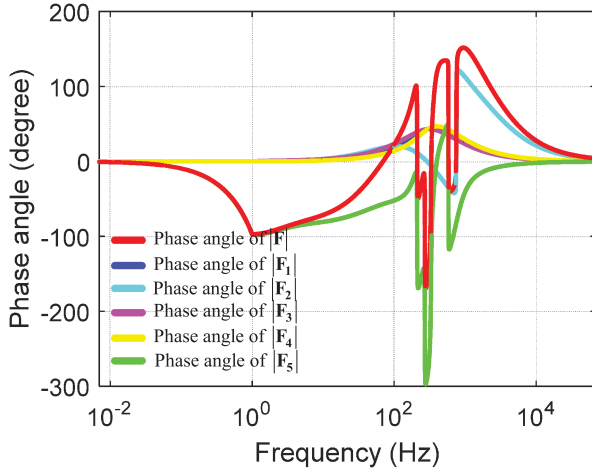


Fig. 4. Phase angles of $|F|$, $|F_1|$, $|F_2|$, $|F_3|$, $|F_4|$, and $|F_5|$ with $k_{pq2} = 1.38 \times 10^{-5}$ and $k_{iq2} = 1.38 \times 10^{-4}$.

controllers [24]. Therefore, to mitigate the instability caused by the dc side, the parameters of the d -axis controllers of the most influential interlinking converter should be tuned to make its dc-side equivalent admittance be positive or less negative.

It is worth noting that depending on the control mode of the interlinking converters, the proposed method may need some modifications to be applicable. To be more specific, when

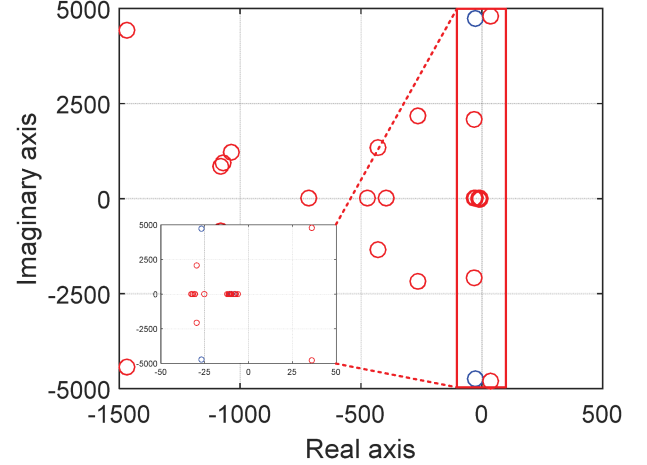


Fig. 5. Pole distribution map of the closed-loop system prior and subsequent to the change of k_{pq2} and k_{iq2} .

the interlinking converters operate under power control (i.e., current control) or droop control mode, the proposed method can be utilized directly without any modification. However, for the interlinking converters operating under dc voltage control mode, the definition of the hybrid ac/dc admittance needs a minor revision, which is clearly elaborated in Section B of the Appendix.

IV. SIMULATION RESULTS

To verify the proposed method, a typical four terminal MTDC system shown in Fig. 2(a) is used as a benchmark system. The interlinking converters are all operating with $P - V_{dc}$ droop control mode with their control diagrams shown in Fig. 2(b). With respect to Fig. 2(b), k_{droop} , k_{pp} , k_{ip} , k_{pq} , k_{iq} , k_{pid} , k_{iid} , k_{piq} , and k_{iiq} represent the droop coefficient, the proportional and integral gains of the active power controller, the proportional and integral gains of the reactive power controller, the proportional and integral gains of the d -axis current controller, respectively. Tables I and II give the main parameters of the test system. Based on the determinant-based GNC, the phase angles within the full positive frequency range, i.e., from 0 Hz to ∞ Hz should be plotted. Due to the computation burden, however, only the frequency range between 0.01 and 50 000 Hz is considered in the following.

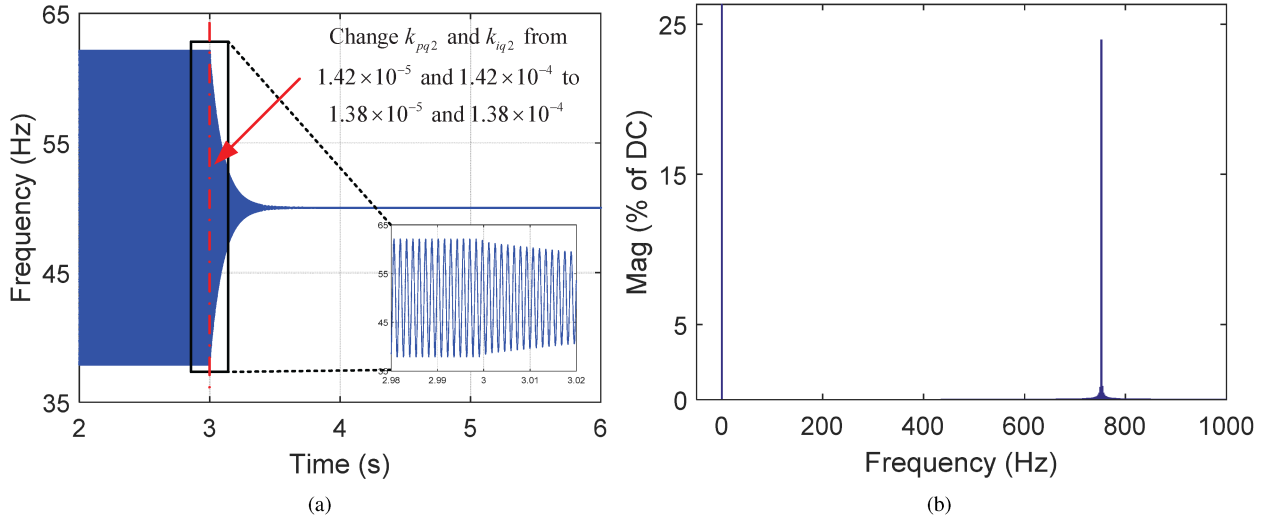


Fig. 6. PLL output frequency waveform of the second interlinking converter and its harmonic spectrum. (a) PLL output frequency waveform of the second interlinking converter with different parameters of the reactive power controller. (b) Harmonic spectrum of the PLL output frequency waveform.

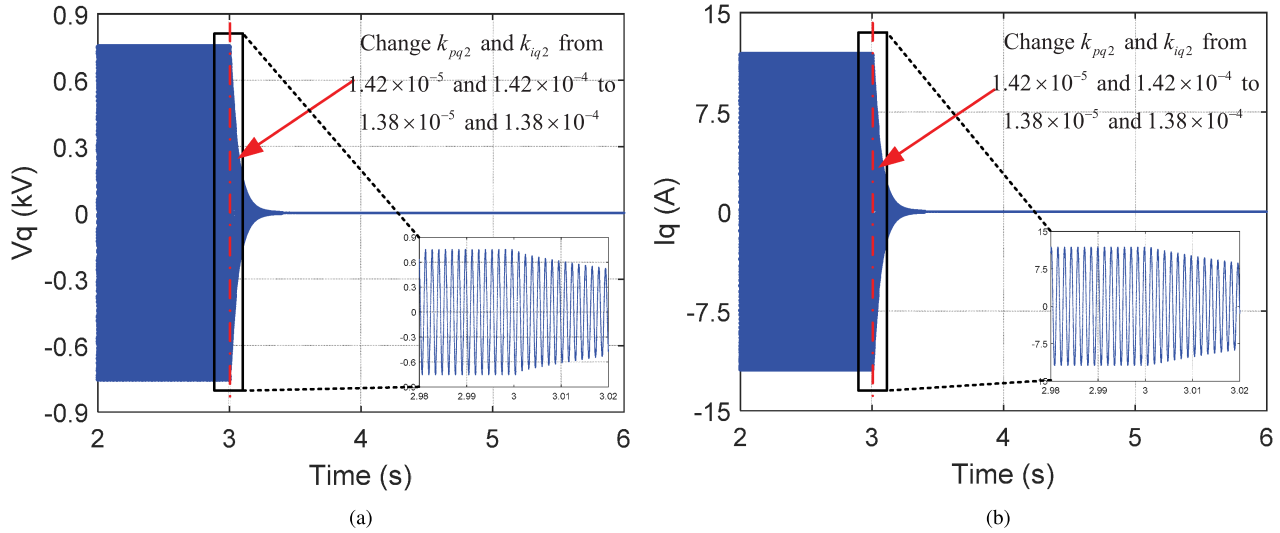


Fig. 7. q -axis voltage and current waveforms of the second interlinking converter with different parameters of the reactive power controller. (a) q -axis voltage waveform. (b) q -axis current waveform.

A. Analysis of System Instability Caused by the AC Side

With parameters listed in Tables I and II, Fig. 3 shows the phase angles of $|\mathbf{F}|$, $|\mathbf{F}_1|$, $|\mathbf{F}_2|$, $|\mathbf{F}_3|$, $|\mathbf{F}_4|$, and $|\mathbf{F}_5|$ within the full positive frequency range. With respect to Fig. 3, when the frequency increases from 0 to infinity, the phase angle of $|\mathbf{F}|$ decreases by 360° . Based on the determinant-based GNC, the closed-loop system contains two RHP poles and the MTDC system is unstable. To further identify the root cause of system instability, the phase angles of $|\mathbf{F}_1|$, $|\mathbf{F}_2|$, $|\mathbf{F}_3|$, $|\mathbf{F}_4|$, and $|\mathbf{F}_5|$ are checked. As demonstrated in Fig. 3, the phase angle decrement of $|\mathbf{F}_5|$ within the entire positive frequency range is 0° , which indicates that the system instability is not caused by the dc side. In contrast, the phase angle of $|\mathbf{F}_2|$ decreases 360° while the phase angle decrements of $|\mathbf{F}_1|$, $|\mathbf{F}_3|$, and $|\mathbf{F}_4|$ are 0° .

According to the analysis presented in Section III-A, the system instability is caused by the ac side of the second interlinking converter.

To mitigate the instability, the q -axis admittance of the second interlinking converter should be reshaped to be positive or less negative. To achieve this goal, the proportional and integral gains of the reactive power controller of the second interlinking converter are diminished from 1.42×10^{-5} and 1.42×10^{-4} to 1.38×10^{-5} and 1.38×10^{-4} , respectively. Correspondingly, the phase angles of $|\mathbf{F}|$, $|\mathbf{F}_1|$, $|\mathbf{F}_2|$, $|\mathbf{F}_3|$, $|\mathbf{F}_4|$, and $|\mathbf{F}_5|$ evolve from Figs. 3 to 4. As shown in Fig. 4, the phase angles of $|\mathbf{F}|$ and $|\mathbf{F}_2|$ change from 360° to 0° . In addition, the phase angles of $|\mathbf{F}_1|$, $|\mathbf{F}_3|$, $|\mathbf{F}_4|$, and $|\mathbf{F}_5|$ remain unchanged. Therefore, subsequent to the parameter change, the MTDC system becomes stable.

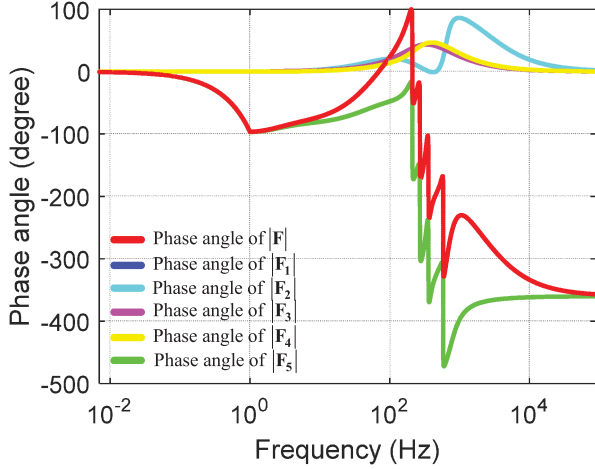


Fig. 8. Phase angles of $|F|$, $|F_1|$, $|F_2|$, $|F_3|$, $|F_4|$, and $|F_5|$ with $k_{pp3} = 0.8 \times 10^{-5}$ and $k_{ip3} = 0.8 \times 10^{-4}$.

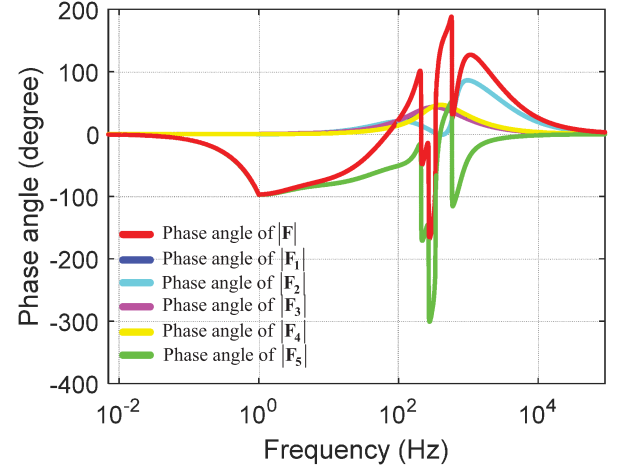


Fig. 10. Phase angles of $|F|$, $|F_1|$, $|F_2|$, $|F_3|$, $|F_4|$, and $|F_5|$ with $k_{pp3} = 0.6 \times 10^{-5}$ and $k_{ip3} = 0.6 \times 10^{-4}$.

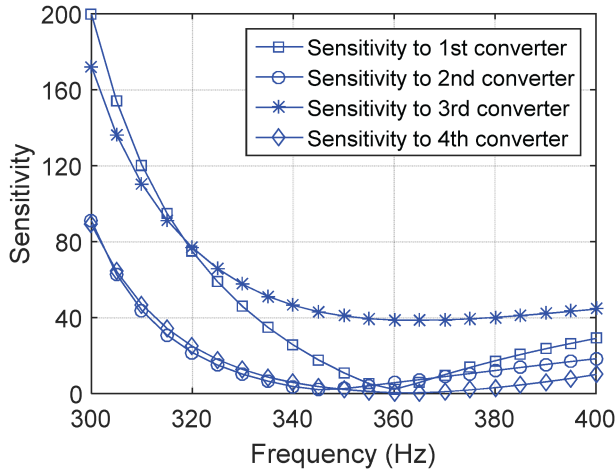


Fig. 9. The sensitivities of $|F_5|$ to the dc-side equivalent admittances of different interlinking converters.

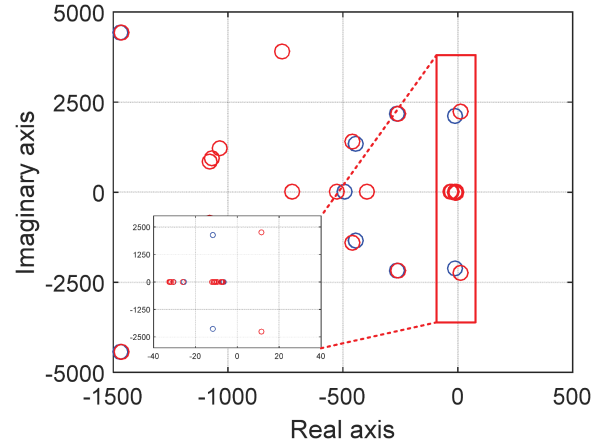


Fig. 11. The pole distribution map of the closed-loop system prior and subsequent to the change of k_{pp3} and k_{ip3} .

Fig. 5 shows the pole distribution maps of the closed-loop system with different parameters. The poles corresponding to Figs. 3 and 4 are marked by red and blue colors, respectively. With respect to Fig. 5, prior to any parameter change, the closed-loop system contains two RHP poles. By comparison, when the proportional and integral gains of the reactive power controller of the second interlinking converter are diminished from 1.42×10^{-5} and 1.42×10^{-4} to 1.38×10^{-5} and 1.38×10^{-4} , all the poles of the closed-loop system are located on the left half plane. Therefore, subsequent to the parameter change, the MTDC system becomes stable, which accords with the system stability assessment results obtained from the proposed method.

Fig. 6(a) shows the PLL output frequency waveform of the second interlinking converter. As shown in Fig. 6(a), prior to the parameter change, the frequency is resonant. Nevertheless, subsequent to the parameter change, the resonance is rapidly attenuated and finally, the frequency comes back to its normal

value. Corresponding to the oscillation part, Fig. 6(b) shows the fast Fourier transform (FFT) analysis results. With respect to Fig. 6(b), prior to the parameter change, the PLL output frequency resonates at around 670 Hz and the harmonic content is about 24%, which conforms to the waveform shown in Fig. 6(a). To further verify the aforementioned analysis results obtained from the proposed method, Fig. 7(a) and (b) demonstrate the q -axis voltage and current waveforms of the second interlinking converter, respectively. As demonstrated in Fig. 7(a) and (b), prior to the parameter change of the reactive power controller, both the q -axis voltage and current have oscillations. In contrast, subsequent to the parameter change, those oscillations rapidly attenuate and finally, both the q -axis voltage and current restore to their nominal values. This is in agreement with the harmonic stability analysis results obtained from Figs. 3, 4, and 5.

B. Analysis of System Instability Caused by the DC Side

Instead of the instability caused by the ac side, this section focuses on the dc-side stability analysis of a MTDC system. While

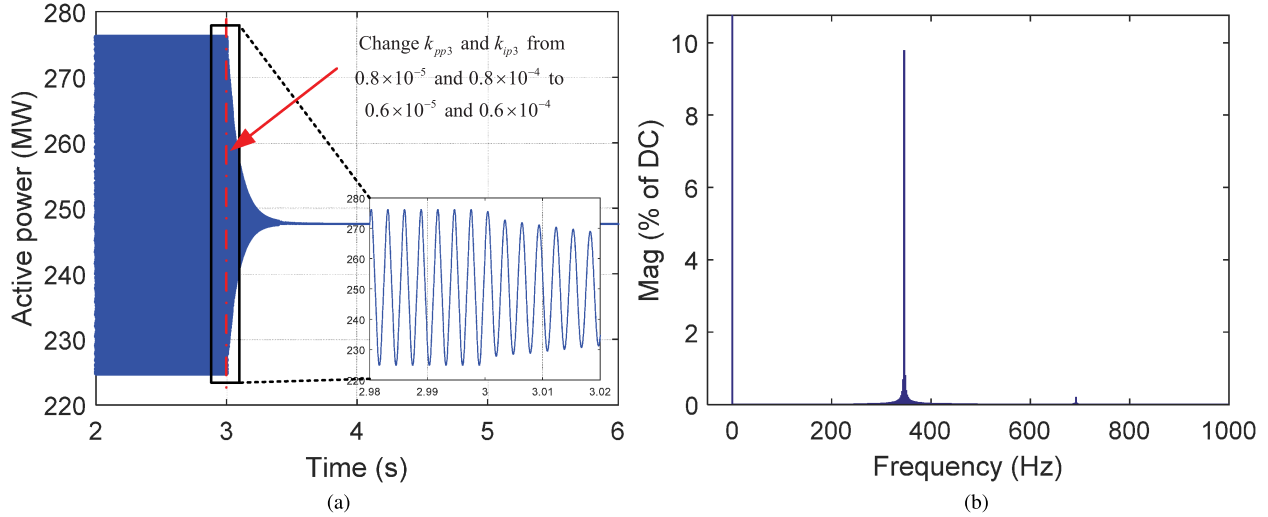


Fig. 12. Output active power waveform of the third interlinking converter and its harmonic spectrum. (a) Output active power waveform of the third interlinking converter with different parameters of the active power controller. (b) Harmonic spectrum of the output active power waveform.

remaining parameters of all other converters stay unchanged, the proportional and integral gains of the active power controller of the third interlinking converter are increased from 0.6×10^{-5} and 0.6×10^{-4} to 0.8×10^{-5} and 0.8×10^{-4} , respectively. With the new parameters, the stability of the MTDC system is restudied in Fig. 8, where the phase angles of $|\mathbf{F}|$, $|\mathbf{F}_1|$, $|\mathbf{F}_2|$, $|\mathbf{F}_3|$, $|\mathbf{F}_4|$, and $|\mathbf{F}_5|$ within the entire positive frequency range are illustrated. With respect to Fig. 8, when the frequency increases from 0 to infinity, the phase angle variations of $|\mathbf{F}_1|$, $|\mathbf{F}_2|$, $|\mathbf{F}_3|$, $|\mathbf{F}_4|$ are 0° while the phase angles of $|\mathbf{F}_5|$ and $|\mathbf{F}|$ decrease by 360° . According to the analysis presented in Sections II-C and III-B, the MTDC system with the new parameters is unstable. Moreover, this instability is caused by the dc side.

To further investigate the key interlinking converter that is responsible for this system instability, (25) is utilized to calculate the sensitivity of $|\mathbf{F}_5|$ with respect to the dc-side equivalent admittance of every interlinking converter. As the phase angle of $|\mathbf{F}|$ decreases by 180° at around 360 Hz and system resonant frequency is around 360 Hz as well, the sensitivity analysis of $|\mathbf{F}_5|$ is conducted in the frequency range between 300 and 400 Hz. Fig. 9 shows the sensitivities of $|\mathbf{F}_5|$ to the dc-side equivalent admittances of different interlinking converters. With respect to Fig. 9, apart from a narrow frequency range between 300 and 315 Hz, the sensitivity of $|\mathbf{F}_5|$ to the dc-side equivalent admittance of the third interlinking converter is always larger than the sensitivities of $|\mathbf{F}_5|$ to those of the other three interlinking converters. Furthermore, in the vicinity of 360 Hz, the sensitivity of $|\mathbf{F}_5|$ to the dc-side equivalent admittance of the third interlinking converter is almost six times to the sensitivities of $|\mathbf{F}_5|$ to those of the other three interlinking converters. Therefore, the dc-side instability is mainly dominated by the third interlinking converter.

By decreasing the proportional and integral gains of the active power controller of the third interlinking converter from 0.8×10^{-5} and 0.8×10^{-4} to 0.6×10^{-5} and 0.6×10^{-4} , the

phase angles of $|\mathbf{F}|$, $|\mathbf{F}_1|$, $|\mathbf{F}_2|$, $|\mathbf{F}_3|$, $|\mathbf{F}_4|$, and $|\mathbf{F}_5|$ are changed from Figs. 8 to 10. As demonstrated in Fig. 10, the phase angles of $|\mathbf{F}_1|$, $|\mathbf{F}_2|$, $|\mathbf{F}_3|$, and $|\mathbf{F}_4|$ remain almost unchanged. However, the phase angle decrements of $|\mathbf{F}|$ and $|\mathbf{F}_5|$ are changed from 360° to 0° . Therefore, the system becomes stable with the new parameters. To validate the stability assessment result obtained from the proposed method, the pole distribution map of the closed-loop system is shown in Fig. 11. The poles corresponding to the system prior and subsequent to the parameter change are marked by the red and blue colors, respectively. As shown in Fig. 11, prior to the parameter change, the closed-loop system contains two RHP poles. In contrast, when the proportional and integral gains of the active power controller of the third interlinking converter are diminished from 0.8×10^{-5} and 0.8×10^{-4} to 0.6×10^{-5} and 0.6×10^{-4} , those two RHP poles move to the left half plane, which indicates that the system is effectively stabilized by this parameter adjustment. Therefore, the system stability results obtained from two different methods are identical and are in agreement with the output active power waveform of the third interlinking converter shown in Fig. 12(a). As shown in Fig. 12(a), when the bandwidth of the active power controller of the third interlinking converter decreases at $t = 3$ s, the oscillation of the output active power of the third interlinking converter gradually attenuates and the system becomes stable. To further analyze the harmonic characteristic, Fig. 12(b) provides the FFT analysis result of the oscillation shown in Fig. 12(a). With respect to Fig. 12(b), prior to the reduction of controller bandwidth, the resonant frequency of the output active power is around 360 Hz, which is consistent with the analysis results deduced from Figs. 8, 11, and 12(a). In addition, the harmonic content of the output active power is about 10%, it is in compliance with the oscillatory waveform shown in Fig. 12(a).

Apart from the output active power waveform, Figs. 13(a), (b), and 14(a) and (b) demonstrate the dc voltage, dc current, d -axis voltage, and d -axis current of the third interlinking

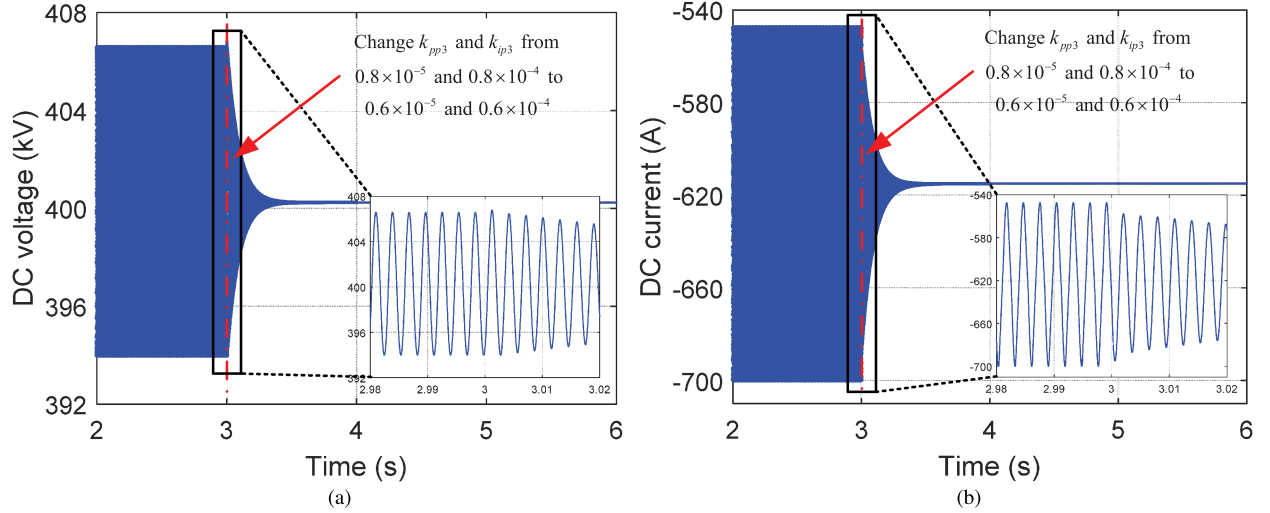


Fig. 13. DC voltage and current waveforms of the third interlinking converter with different parameters of the active power controller. (a) DC voltage waveform. (b) DC current waveform.

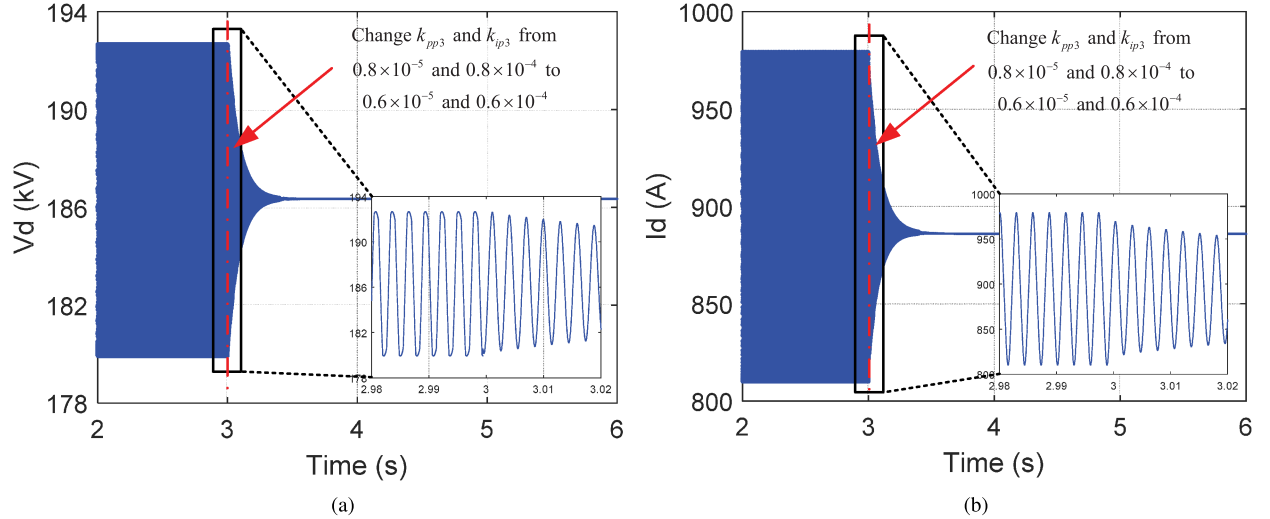


Fig. 14. d -axis voltage and current waveforms of the third interlinking converter with different parameters of the active power controller. (a) d -axis voltage waveform. (b) d -axis current waveform.

converter with different parameters of the active power controller, respectively. As shown in Figs. 13 and 14, prior to the parameter change, the four aforementioned variables remain oscillatory. However, subsequent to the parameter change, the oscillations are successfully mitigated and correspondingly, the MTDC system becomes stable again.

V. CONCLUSION

This article focuses on the stability analysis of MTDC systems. To this end, this article first establishes the stability assessment model for a MTDC system based on the hybrid ac/dc admittance. Then, the determinant-based GNC is introduced to assess the system stability and analyze different system instability root causes including the ac side, the dc side, and the

coupling interaction between the ac and dc sides. Regarding the instability caused by the ac side, this article utilizes the phase angle variation of $|\mathbf{F}_i| (i = 1, 2, \dots, n)$ to identify the dominant interlinking converter that triggers system instability. In contrast, for the instability caused by the dc side or the coupling interaction, a sensitivity analysis is conducted to recognize the most influential interlinking converter that causes the dc-side instability. Subsequent to the identification of system instability root causes, this article provides the corresponding instability mitigation methods. To be more specific, the instability caused by the ac or dc side should be mitigated by reshaping the q -axis admittance or the dc-side equivalent admittance of the dominant interlinking converter, respectively. Finally, the proposed method is verified by the simulation studies in the MATLAB/Simulink environment.

APPENDIX

A. Main Parameters of the Test System

TABLE I
MAIN PARAMETERS OF THE INTERLINKING CONVERTERS OF
THE STUDY SYSTEM

Symbol	Description	Value
V_{dc}	Rated DC voltage	400 kV
V_{ac}	Rated AC voltage	220 kV
L_c	Inductance of the converter filter	40 mH
R_c	Resistance of the converter filter	1.26 Ω
ω	Line frequency of the AC grid	100 π rad/s
k_{droop}	Droop coefficient	10000
k_{ppll}	Proportional gain of the PLL	0.01
k_{ipll}	Integral gain of the PLL	0.1
k_{pp}	Proportional gain of the active power controller	0.6×10^{-5}
k_{ip}	Integral gain of the active power controller	0.6×10^{-4}
k_{pq}	Proportional gain of the reactive power controller	1.42×10^{-5}
k_{iq}	Integral gain of the reactive power controller	1.42×10^{-4}
k_{pid}	Proportional gain of the d -axis current loop	5.03
k_{iid}	Integral gain of the d -axis current loop	158.34
k_{piq}	Proportional gain of the q -axis current loop	5.03
k_{iiq}	Integral gain of the q -axis current loop	158.34

TABLE II
MAIN PARAMETERS OF THE STUDY SYSTEM

Symbol	Description	Value
V_{dc}	DC voltage of the DC network	400 kV
V_{ac}	AC voltage of the AC grid	220 kV
f_{ac}	Line frequency of the AC grid	50 Hz
L_{s1}	Inductance of the 1 st AC grid	40 mH
R_{s1}	Resistance of the 1 st AC grid	1.26 Ω
L_{s2}	Inductance of the 2 nd AC grid	40 mH
R_{s2}	Resistance of the 2 nd AC grid	0.5 Ω
L_{s3}	Inductance of the 3 rd AC grid	40 mH
R_{s3}	Resistance of the 3 rd AC grid	1.26 Ω
L_{s4}	Inductance of the 4 th AC grid	40 mH
R_{s4}	Resistance of the 4 th AC grid	1.26 Ω
l_{12}	Length of the DC line between nodes 1 and 2	184.4 km
l_{23}	Length of the DC line between nodes 2 and 3	101 km
l_{34}	Length of the DC line between nodes 3 and 4	131.1 km
l_{14}	Length of the DC line between nodes 1 and 4	78.3 km
R_0	Resistance of the DC line per unit length	0.01273 Ω/km
L_0	Inductance of the DC line per unit length	0.9337 mH/km
C_0	Capacitance of the DC line per unit length	0.01274 $\mu\text{F}/\text{km}$

B. Modification of the Proposed Method When Interlinking Converters Operate Under DC Voltage Control Mode

When interlinking converters operate under dc voltage control mode, the general assumption that all the interlinking converters are stable when they operate standalone, cannot guarantee that their hybrid ac/dc admittances do not contain any RHP pole. Consequently, the hybrid ac/dc admittance matrix of the second subsystem, i.e., \mathbf{Y}_{sub2} may contain RHP poles as well and the proposed method may become inapplicable. To extend the applicability of the proposed method to the interlinking converters operating under dc voltage control mode, the definition of the hybrid ac/dc admittance model needs a minor revision. To be

more specific, when an interlinking converter operates under dc voltage control mode, its hybrid ac/dc admittance can be defined by

$$\begin{bmatrix} \tilde{i}_d \\ \tilde{i}_q \\ \tilde{v}_{dc} \end{bmatrix} = \begin{bmatrix} \mathbf{Y}_{\text{con}}^{\text{ac}} & \mathbf{Z}_{\text{con}}^{\text{acdc}} \\ \mathbf{Y}_{\text{con}}^{\text{dcac}} & \mathbf{Z}_{\text{con}}^{\text{dc}} \end{bmatrix} \begin{bmatrix} \tilde{v}_d \\ \tilde{v}_q \\ \tilde{i}_{dc} \end{bmatrix} \quad (26)$$

where $\mathbf{Y}_{\text{con}}^{\text{ac}}$, $\mathbf{Z}_{\text{con}}^{\text{acdc}}$, $\mathbf{Y}_{\text{con}}^{\text{dcac}}$, and $\mathbf{Z}_{\text{con}}^{\text{dc}}$ represent the ac admittance matrix, the coupling impedance matrix between the ac and dc sides, the coupling admittance matrix between the ac and dc sides, and the dc impedance of the interlinking converter, respectively. The former three matrices are defined as follows:

$$\mathbf{Y}_{\text{con}}^{\text{ac}} = \begin{bmatrix} Y_{dd}^c & Y_{dq}^c \\ Y_{qd}^c & Y_{qq}^c \end{bmatrix} \quad (27)$$

$$\mathbf{Z}_{\text{con}}^{\text{acdc}} = [Z_{ddc}^c \ Z_{qdc}^c]^T \quad (28)$$

$$\mathbf{Y}_{\text{con}}^{\text{dcac}} = [Y_{dcd}^c \ Y_{dcq}^c] \quad (29)$$

By comparison with the conventional hybrid ac/dc admittance defined by (10), the inputs and outputs of the newly defined hybrid ac/dc admittance are changed from $[\tilde{v}_d \ \tilde{v}_q \ \tilde{v}_{dc}]^T$ and $[\tilde{i}_d \ \tilde{i}_q \ \tilde{i}_{dc}]^T$ to $[\tilde{v}_d \ \tilde{v}_q \ \tilde{i}_{dc}]^T$ and $[\tilde{i}_d \ \tilde{i}_q \ \tilde{v}_{dc}]^T$. It is worth to note that although the off-diagonal elements of the hybrid ac/dc admittance defined by (26) are represented by $\mathbf{Z}_{\text{con}}^{\text{acdc}}$ and $\mathbf{Y}_{\text{con}}^{\text{dcac}}$, they are neither impedances nor admittances. Instead, according to their definitions, they just represent the couplings between the ac admittance matrix and the dc impedance of the interlinking converter, i.e., $\mathbf{Y}_{\text{con}}^{\text{ac}}$ and $\mathbf{Z}_{\text{con}}^{\text{dc}}$. For consistency with the other notations, they are still represented by $\mathbf{Z}_{\text{con}}^{\text{acdc}}$ and $\mathbf{Y}_{\text{con}}^{\text{dcac}}$, respectively. On this basis, with the general assumption that the interlinking converter is stable when it operates standalone, the newly defined hybrid ac/dc admittance does not contain any RHP pole and, consequently, the proposed method becomes applicable again to the interlinking converter operating under dc voltage control mode.

In order to demonstrate this, a three-terminal dc system shown in Fig. 15 is introduced. With respect to Fig. 15, the first interlinking converter operates under dc voltage control mode while the other two interlinking converters operate under P/Q control mode. By labeling the variables related to the i th interlinking converter with subscript “ i ,” u_{abci} , v_{abci} , i_{abci} , v_{dci} , and i_{dci} represent the three-phase voltages of the i th ac grid, the ac-side phase voltage of the i th interlinking converter at its PCC, the grid current of the i th ac grid, the dc-side PCC voltage of the i th interlinking converter, and the dc current of the i th interlinking converter, respectively. To assess the stability of the three-terminal dc system, from the PCCs on the ac and dc sides of the interlinking converters, the whole system is initially divided into three parts, i.e., the ac grids, the dc network, and the interlinking converters. The former two parts constitute the first subsystem while the interlinking converters are regrouped as the second subsystem. After defining the d -axis and q -axis components of u_{abci} , v_{abci} , and i_{abci} in the d - q synchronous reference frame as u_{di} , u_{qi} , v_{di} , v_{qi} , i_{di} , and i_{qi} , respectively, the three-terminal dc system is modeled in the following.

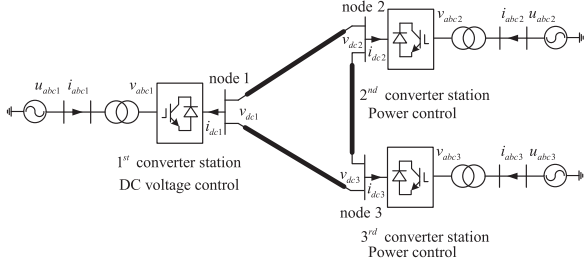


Fig. 15. Circuit diagram of a three-terminal dc system.

With respect to Fig. 15, the dc network is described by

$$\begin{bmatrix} \tilde{i}_{dc1} \\ \tilde{v}_{dc2} \\ \tilde{v}_{dc3} \end{bmatrix} = \begin{bmatrix} Y_{net11}^{dc} & Z_{net12}^{dc} & Z_{net13}^{dc} \\ Y_{net21}^{dc} & Z_{net22}^{dc} & Z_{net23}^{dc} \\ Y_{net31}^{dc} & Z_{net32}^{dc} & Z_{net33}^{dc} \end{bmatrix} \begin{bmatrix} -\tilde{v}_{dc1} \\ -\tilde{i}_{dc2} \\ -\tilde{i}_{dcn} \end{bmatrix} \quad (30)$$

where \tilde{i}_{dc1} , \tilde{v}_{dc2} , \tilde{v}_{dc3} , \tilde{v}_{dc1} , \tilde{i}_{dc2} , and \tilde{i}_{dcn} represent the small-signal values of i_{dc1} , v_{dc2} , v_{dc3} , v_{dc1} , i_{dc2} , and i_{dcn} , respectively. In addition, by mapping the i th ac grid to the synchronous reference frame, its small-signal representation is expressed by

$$\begin{bmatrix} \tilde{u}_{di} \\ \tilde{u}_{qi} \end{bmatrix} - \mathbf{Z}_{gridi}^{ac} \begin{bmatrix} \tilde{i}_{di} \\ \tilde{i}_{qi} \end{bmatrix} = \begin{bmatrix} \tilde{v}_{di} \\ \tilde{v}_{qi} \end{bmatrix} \quad (i = 1, 2, 3) \quad (31)$$

where \tilde{u}_{di} , \tilde{u}_{qi} , \tilde{v}_{di} , \tilde{v}_{qi} , \tilde{i}_{di} , and \tilde{i}_{qi} represent the small-signal values of u_{di} , u_{qi} , v_{di} , v_{qi} , i_{di} , and i_{qi} , respectively. \mathbf{Z}_{gridi}^{ac} represents the impedance matrix of the i th ac grid. On the basis of (30) and (31), the first subsystem is modeled by

$$\tilde{\mathbf{u}}_{acdc} = \mathbf{Z}_{sub1} \tilde{\mathbf{i}}_{acdc} + \tilde{\mathbf{v}}_{acdc} \quad (32)$$

where $\tilde{\mathbf{u}}_{acdc}$, $\tilde{\mathbf{i}}_{acdc}$, $\tilde{\mathbf{v}}_{acdc}$, and \mathbf{Z}_{sub1} are defined as

$$\tilde{\mathbf{u}}_{acdc} = [\tilde{u}_{d1} \ \tilde{u}_{q1} \ \tilde{u}_{d2} \ \tilde{u}_{q2} \ \tilde{u}_{d3} \ \tilde{u}_{q3} \ 0 \ 0 \ 0]^T \quad (33)$$

$$\tilde{\mathbf{i}}_{acdc} = [\tilde{i}_{d1} \ \tilde{i}_{q1} \ \tilde{i}_{d2} \ \tilde{i}_{q2} \ \tilde{i}_{d3} \ \tilde{i}_{q3} \ \tilde{v}_{dc1} \ \tilde{i}_{dc2} \ \tilde{i}_{dc3}]^T \quad (34)$$

$$\tilde{\mathbf{v}}_{acdc} = [\tilde{v}_{d1} \ \tilde{v}_{q1} \ \tilde{v}_{d2} \ \tilde{v}_{q2} \ \tilde{v}_{d3} \ \tilde{v}_{q3} \ \tilde{i}_{dc1} \ \tilde{v}_{dc2} \ \tilde{v}_{dc3}]^T \quad (35)$$

$$\mathbf{Z}_{sub1} = \begin{bmatrix} \mathbf{Z}_{grid1}^{ac} & 0 & 0 & 0 & 0 & 0 \\ 0 & \mathbf{Z}_{grid2}^{ac} & 0 & 0 & 0 & 0 \\ 0 & 0 & \mathbf{Z}_{grid3}^{ac} & 0 & 0 & 0 \\ 0 & 0 & 0 & Y_{net11}^{dc} & Z_{net12}^{dc} & Z_{net13}^{dc} \\ 0 & 0 & 0 & Y_{net21}^{dc} & Z_{net22}^{dc} & Z_{net23}^{dc} \\ 0 & 0 & 0 & Y_{net31}^{dc} & Z_{net32}^{dc} & Z_{net33}^{dc} \end{bmatrix} \quad (36)$$

According to the newly defined hybrid ac/dc admittance, the first interlinking converter, i.e., the one operating under dc voltage control mode is described by

$$\begin{bmatrix} \tilde{i}_{d1} \\ \tilde{i}_{q1} \\ \tilde{v}_{dc1} \end{bmatrix} = \begin{bmatrix} \mathbf{Y}_{con1}^{ac} & \mathbf{Z}_{con1}^{acdc} \\ \mathbf{Y}_{con1}^{dcac} & \mathbf{Z}_{con1}^{dc} \end{bmatrix} \begin{bmatrix} \tilde{v}_{d1} \\ \tilde{v}_{q1} \\ \tilde{i}_{dc1} \end{bmatrix} \quad (37)$$

In addition, the second and third interlinking converters, i.e., the ones operating under power control modes are described by

$$\begin{bmatrix} \tilde{i}_{di} \\ \tilde{i}_{qi} \\ \tilde{i}_{dci} \end{bmatrix} = \begin{bmatrix} \mathbf{Y}_{con1}^{ac} & \mathbf{Y}_{con1}^{acdc} \\ \mathbf{Y}_{con1}^{dcac} & \mathbf{Y}_{con1}^{dc} \end{bmatrix} \begin{bmatrix} \tilde{v}_{di} \\ \tilde{v}_{qi} \\ \tilde{v}_{dci} \end{bmatrix} \quad (i = 2, 3). \quad (38)$$

Then, with the variables defined in (37) and (38), the second subsystem is modeled by

$$\tilde{\mathbf{i}}_{acdc} = \mathbf{Y}_{sub2} \tilde{\mathbf{v}}_{acdc} \quad (39)$$

where \mathbf{Y}_{sub2} is defined by

$$\mathbf{Y}_{sub2} = \begin{bmatrix} \mathbf{Y}_{con1}^{ac} & 0 & 0 & \mathbf{Z}_{con1}^{acdc} & 0 & 0 \\ 0 & \mathbf{Y}_{con2}^{ac} & 0 & 0 & \mathbf{Y}_{con2}^{acdc} & 0 \\ 0 & 0 & \mathbf{Y}_{con3}^{ac} & 0 & 0 & \mathbf{Y}_{con3}^{acdc} \\ \mathbf{Y}_{con1}^{dcac} & 0 & 0 & \mathbf{Z}_{con1}^{dc} & 0 & 0 \\ 0 & \mathbf{Y}_{con2}^{dcac} & 0 & 0 & \mathbf{Y}_{con2}^{dc} & 0 \\ 0 & 0 & \mathbf{Y}_{con3}^{dcac} & 0 & 0 & \mathbf{Y}_{con3}^{dc} \end{bmatrix} \quad (40)$$

By substituting for the current from (39) into (32), the three-terminal dc system is modeled by

$$\tilde{\mathbf{v}}_{acdc} = (\mathbf{I} + \mathbf{Z}_{sub1} \mathbf{Y}_{sub2})^{-1} \tilde{\mathbf{u}}_{acdc} \quad (41)$$

Corresponding to (41), the system minor-loop gain can be defined as

$$\mathbf{L} = \mathbf{Z}_{sub1} \mathbf{Y}_{sub2} \quad (42)$$

and the stability can be determined by the determinant of the return-difference matrix expressed by

$$|\mathbf{F}| = |\mathbf{I} + \mathbf{L}| = |\mathbf{I} + \mathbf{Z}_{sub1} \mathbf{Y}_{sub2}| \quad (43)$$

The following steps including the identification of system instability root cause and the mitigation of system instability are similar to the process presented in Section III. Therefore, based on the aforementioned discussion, the method proposed in the article is still universal for the MTDC systems with interlinking converters operating under dc voltage control modes.

REFERENCES

- [1] N. Chaudhuri, B. Chaudhuri, R. Majumder, and A. Yazdani, *Multi-Terminal Direct-Current Grids: Modeling, Analysis, and Control*. Hoboken, NJ, USA: Wiley, 2014.
- [2] J. Beerten, S. Cole, and R. Belmans, "Generalized steady-state VSC MTDC model for sequential AC/DC power flow algorithms," *IEEE Trans. Power Syst.*, vol. 27, no. 2, pp. 821–829, May 2012.
- [3] W. Lu and B.-T. Ooi, "Optimal acquisition and aggregation of offshore wind power by multiterminal voltage-source HVDC," *IEEE Trans. Power Del.*, vol. 18, no. 1, pp. 201–206, Jan. 2003.
- [4] X. Wang and F. Blaabjerg, "Harmonic stability in power electronic based power systems: Concept, modeling, and analysis," *IEEE Trans. Smart Grid*, vol. 10, no. 3, pp. 2858–2870, May 2019.
- [5] J. Sun, G. Wang, X. Du, and H. Wang, "A theory for harmonics created by resonance in converter-grid systems," *IEEE Trans. Power Electron.*, vol. 34, no. 4, pp. 3025–3029, Apr. 2019.
- [6] Z. Li and M. Shahidehpour, "Small-signal modeling and stability analysis of hybrid AC/DC microgrids," *IEEE Trans. Smart Grid*, vol. 10, no. 2, pp. 2080–2095, Mar. 2019.
- [7] P. Kundur, N. J. Balu, and M. G. Lauby, *Power System Stability and Control*. New York, NY, USA: McGraw-Hill, 1994.
- [8] R. D. Middlebrook, "Input filter considerations in design and application of switching regulators," in *Proc. IEEE Ind. Appl. Soc. Annu. Meeting*, 1976, pp. 94–107.
- [9] M. Belkhat, "Stability criteria for AC power systems with regulated loads," Ph.D. dissertation, Purdue Univ. West Lafayette, IN, USA, 1997.
- [10] J. Sun, "Impedance-based stability criterion for grid-connected inverters," *IEEE Trans. Power Electron.*, vol. 26, no. 11, pp. 3075–3078, Nov. 2011.
- [11] B. Wen, D. Boroyevich, R. Burgos, P. Mattavelli, and Z. Shen, "Analysis of DQ small-signal impedance of grid-tied inverters," *IEEE Trans. Power Electron.*, vol. 31, no. 1, pp. 675–687, Jan. 2016.

- [12] B. Wen, D. Boroyevich, R. Burgos, P. Mattavelli, and Z. Shen, "Small-signal stability analysis of Three-phase AC systems in the presence of constant power loads based on measured d-q frame impedances," *IEEE Trans. Power Electron.*, vol. 30, no. 10, pp. 5952–5963, Oct. 2015.
- [13] C. Zou *et al.*, "Analysis of resonance between a VSC-HVDC converter and the AC grid," *IEEE Trans. Power Electron.*, vol. 33, no. 12, pp. 10157–10168, Dec. 2018.
- [14] J. Zhu, J. Hu, L. Lin, Y. Wang, and C. Wei, "High-frequency oscillation mechanism analysis and suppression method of VSC-HVDC," *IEEE Trans. Power Electron.*, vol. 35, no. 9, pp. 8892–8896, Sep. 2020.
- [15] J. Sun, "Autonomous local control and stability analysis of multiterminal DC systems," *IEEE Trans. Emerg. Sel. Topics Power Electron.*, vol. 3, no. 4, pp. 1078–1089, Dec. 2015.
- [16] W. Wu *et al.*, "A virtual phase-lead impedance stability control strategy for the maritime VSC-HVDC system," *IEEE Trans. Ind. Inform.*, vol. 14, no. 12, pp. 5475–5486, Dec. 2018.
- [17] G. Pinares and M. Bongiorno, "Methodology for the analysis of DC-network resonance-related instabilities in voltage-source converter-based multi-terminal HVDC systems," *IET Gener., Transmiss. Distrib.*, vol. 12, no. 1, pp. 170–177, 2018.
- [18] M. Amin, M. Molinas, J. Lyu, and X. Cai, "Impact of power flow direction on the stability of VSC-HVDC seen from the impedance nyquist plot," *IEEE Trans. Power Electron.*, vol. 32, no. 10, pp. 8204–8217, Oct. 2017.
- [19] G. Pinares and M. Bongiorno, "Modeling and analysis of VSC-based HVDC systems for DC network stability studies," *IEEE Trans. Power Del.*, vol. 31, no. 2, pp. 848–856, Apr. 2016.
- [20] Y. Liao and X. Wang, "Impedance-based stability analysis for interconnected converter systems with open-loop RHP poles," *IEEE Trans. Power Electron.*, vol. 35, no. 4, pp. 4388–4397, Apr. 2020.
- [21] L. Fan and Z. Miao, "Admittance-based stability analysis: Bode plots, Nyquist diagrams or eigenvalue analysis?," *IEEE Trans. Power Syst.*, vol. 35, no. 4, pp. 3312–3315, Jul. 2020.
- [22] C. Zhang, X. Cai, M. Molinas, and A. Rygg, "On the impedance modeling and equivalence of AC/DC-side stability analysis of a grid-tied type-IV wind turbine system," *IEEE Trans. Energy Convers.*, vol. 34, no. 2, pp. 1000–1009, Jun. 2019.
- [23] H. Zhang, M. Mehrabankhomartash, M. Saeedifard, Y. Zou, Y. Meng, and X. Wang, "Impedance analysis and stabilization of point-to-point HVDC systems based on a hybrid AC/DC impedance model," *IEEE Trans. Ind. Electron.*, vol. 68, no. 4, pp. 3224–3238, Apr. 2021.
- [24] J. Pedra, L. Sainz, and L. Monjo, "Three-port small signal admittance-based model of VSCs for studies of multi-terminal HVDC hybrid AC/DC transmission grids," *IEEE Trans. Power Syst.*, vol. 36, no. 1, pp. 732–743, Jan. 2021.
- [25] W. Cao, Y. Ma, L. Yang, F. Wang, and L. M. Tolbert, "D-Q impedance based stability analysis and parameter design of Three-phase inverter-based AC power systems," *IEEE Trans. Ind. Electron.*, vol. 64, no. 7, pp. 6017–6028, Jul. 2017.
- [26] W. Cao, Y. Ma, and F. Wang, "Sequence-impedance-based harmonic stability analysis and controller parameter design of Three-phase inverter-based multibus AC power systems," *IEEE Trans. Power Electron.*, vol. 32, no. 10, pp. 7674–7693, Oct. 2017.
- [27] J. Skogestad and I. Postlethwaite, *Multivariable Feedback Control: Analysis and Design*. New York, NY, USA: Wiley, 2007.
- [28] J. Fang, X. Li, H. Li, and Y. Tang, "Stability improvement for Three-phase grid-connected converters through impedance reshaping in quadrature-axis," *IEEE Trans. Power Electron.*, vol. 33, no. 10, pp. 8365–8375, Oct. 2018.



Haitao Zhang (Student Member, IEEE) received the B.S. degree in electrical engineering from the Zhejiang University, Hangzhou, China, in 2014, and the Ph.D. degree in electrical engineering from the Xi'an Jiaotong University, Xi'an, Shaanxi, China, in 2021, respectively.

From 2018 to 2019, he was a Visiting Scholar with the School of Electrical and Computer Engineering, Georgia Institute of Technology, Atlanta, GA, USA. He is currently as Assistant Professor in the School of Electrical Engineering, Xi'an Jiaotong University,

Xi'an, Shaanxi, China. His research interests include stability analysis of hybrid ac/dc power system, space vector modulation (SVPWM) for multilevel converter, and control of MMC-based MTDC system.



Xiuli Wang (Senior Member, IEEE) received the B.S., M.S., and Ph.D. degrees in electrical engineering from Xi'an Jiaotong University, Xi'an China, in 1982, 1985, and 1997, respectively.

She has been with Xi'an Jiaotong University since 1985, where she is currently a Professor with School of Electrical Engineering. Her research interests include the power market, reliability assessment of power system, and integration of renewable power.



Mahmoud Mehrabankhomartash (Student Member, IEEE) received the B.Sc. and M.Sc. degrees in electrical engineering from Sharif University of Technology, Tehran, Iran, in 2013 and 2015, respectively. He is currently working toward the Ph.D. degree with the School of Electrical and Computer Engineering, Georgia Institute of Technology, Atlanta, GA, USA.

His research interests include high voltage dc (HVDC) systems and power electronics.



Maryam Saeedifard (Senior Member, IEEE) received the Ph.D. degree in electrical engineering from the University of Toronto, Toronto, Canada, in 2008.

She is currently as Associate Professor with the School of Electrical and Computer Engineering, Georgia Institute of Technology, Atlanta, GA, USA. Prior joining Georgia Tech, she was an Assistant Professor with the School of Electrical and Computer Engineering, Purdue University, West Lafayette, IN, USA. Her research interests include power electronics and applications of power electronics in power

systems.



Yongqing Meng received the Ph.D. degree in electrical engineering from Xi'an Jiaotong University, Xi'an, China, in 2007.

He is currently a Lecturer with the School of Electrical Engineering, Xian Jiaotong University. His research interests include renewable energy generation, HVDC transmission systems, fractional frequency transmission systems, FACTS, and stability analysis and control of power system.



Xifan Wang (Life Fellow, IEEE) received the bachelor's degree in electrical engineering from Xi'an Jiaotong University, Xi'an, China, in 1957.

From 1983 to 1986, he was a Visiting Scientist with Cornell University, Ithaca, NY, USA. From 1991 to 1994, he was a Visiting Professor with the Kyushu Institute of Technology, Kitakyushu, Japan. He is currently a member of the Chinese Academy of Science, Beijing, China. He is currently a Director of the Research Institute of Power Systems, Xi'an Jiaotong University. His current research interests include the

analysis, operation and planning of power systems, and novel transmission schemes.